DOI: 10.13009/EUCASS2017-656

Direct Numerical Simulation of Transitional Boundary Layer with Local Separation in Hypersonic Flight

Andrey V. Novikov ***
** Moscow Institute of Physics and Technology (MIPT)*
9 Institutskiy per., Dolgoprudny, Russia, 141701
*** Central Aerohydrodynamic Institute (TsAGI)*
1 Zhukovsky Street, Zhukovsky, Russia, 140180

Abstract
Direct numerical simulation of laminar-turbulent transition in the boundary layer over a long 5.5 degree slopped plate at the freestream Mach number 5.373 is carried out. The transition is induced by artificial three-dimensional unsteady disturbances generated in the near-wall flow using a local suction-blowing actuator in pulsed or periodic regime. The simulation is done by numerically integrating the three-dimensional unsteady Navier–Stokes equations using the in-house HSFlow solver, which implements an implicit finite-volume shock-capturing method with the 2nd order approximation in time and effectively 3rd order in space. The undisturbed laminar boundary layer separates upstream of the corner line and forms a shallow separation zone. The actuator generates three-dimensional disturbances propagating downstream. The disturbances grow monotonically and pass through linear, nonlinear and breakdown stages. In the linear stage upstream the separation zone, the disturbance is dominated by oblique waves of the first mode. In the breakdown stage in the reattached boundary layer "young" turbulent spot or wedge are formed depending on the actuator regime. The transitional boundary layer exhibits small-scale hairpin vortices, acoustic noise emanating outside, increased heat transfer. This numerical simulation may help to setup and perform controlled stability experiments in wind tunnels as well as develop holistic models of transitional boundary layer at hypersonic speeds.

1. Introduction

Laminar-turbulent transition (LTT) in hypersonic boundary-layer flows is one of the major unsolved problems of high-speed flight physics. Since LTT leads to significant increases in heat transfer, reliable estimates of LTT locations are needed to predict the aero-thermal loads and surface temperatures. LTT also significantly effects on the aerodynamic performance because of a substantial increase of the skin friction. In the case of low free-stream disturbances typical for flight conditions, LTT includes the three main stages [1]: receptivity to external disturbances; growth of unstable modes; nonlinear breakdown of disturbances leading to a fully turbulent flow regime. Physical mechanisms relevant to these stages should be studied using theoretical, experimental and numerical approaches. However, even after many years of research still very little is known regarding the nonlinear stages of transition.
Direct numerical simulations (DNS) are well suited for a holistic modelling of the all LTT stages including nonlinear breakdown. The modern methods of parallel computations using supercomputers make it feasible to conduct such numerical studies for relatively simple configurations like flat plates and sharp cones at zero angle of attack [2, 3]. However, in many practical cases we are dealing with transition in locally separated boundary layers. One of the most typical configurations is a compression corner, where the interaction between the oncoming boundary layer and the adverse pressure gradient drastically modifies the mean flow field.
In this paper presented are some results of DNS of artificially excited 3D disturbances that induce LTT in the near-wall flow over 5.5 degree sloped plate at the freestream Mach number 5.373 and unit Reynolds number $Re_{\infty,1} = 17.9\times10^6$ m^{-1}. This configuration and free-stream parameters are relevant to the NASA X-43 hypersonic glider model tested in the NASA LaRC 20-Inch Mach 6 Air Tunnel [4]. The earlier stability and numerical studies under these free-stream conditions were performed for 2D [5, 6] and 3D disturbances [7 – 11]. The disturbances are introduced via forcing of suction–blowing type through a small hole on the wall. The 3D Navier–Stokes equations for unsteady compressible flows of viscous perfect gas are solved using the in-house solver "HSFlow" (High Speed Flow) that implements implicit finite-volume shock-capturing method. Main features of instability development in the linear and nonlinear stages are explored using instant wall disturbance fields, shadowgraphs of disturbed

DOI: 10.13009/EUCASS2017-656

boundary layer and visualizations of 3D vortices. Distribution of the heat transfer coefficient helps to detect the beginning of LTT and estimate the length of transitional region.

2. Problem formulation and numerical method

2.1 Governing equations

The equations to be solved are the 3D unsteady Navier–Stokes equations in conservative dimensionless form. The fluid is a perfect gas with the specific heat ratio $\gamma = 1.4$ and Prandtl number Pr = 0.72. The dynamic viscosity is calculated using Sutherland's law $\mu = T^{3/2}\left(S+1\right)/\left(S+T\right)$, where $S = 110\,\mathrm{K}/T_\infty^*$. The bulk viscosity is assumed to be zero. The coordinates are normalized to the reference length L^* that is the distance from the leading edge to the corner point. The dependent variables are normalized to the corresponding freestream parameters, and pressure – to the doubled dynamic pressure $\rho_\infty^* U_\infty^{*2}$. Hereafter asterisks denote dimensional quantities. The details of the governing equations used for the DNS may be found in e.g. [12].

2.2 Numerical method

The Navier–Stokes equations are integrated using the in-house solver HSFlow (High Speed Flow), which implements an implicit finite-volume shock-capturing method with the second-order approximation in space and time. Godunov-type TVD scheme with Roe approximate Riemann solver is used. Reconstruction of dependent variables at the grid cell boundaries is performed using WENO (Weighted Essentially Non-Oscillatory) approach, which effectively gives the third-order space approximation. The system of nonlinear algebraic equations, which approximates the governing partial differential equations, is solved using the Newton iteration method. At every iteration step, the corresponding linear algebraic system is solved using the GMRes (Generalized Minimal Residual) method. This approach is universal and most efficient if the computational domain contains shock waves and other strong spatial inhomogeneities of the flow, such as boundary-layer separation.
The HSFlow solver employs MPI technology and PETSc framework for distributed calculations on high-performance computing clusters. For parallel computations, the source structured grid is split into multiple zones with one-to-one interzone connectivity. The discretization is done in each zone independently and fully parallel. The resulting algebraic equations are solved collectively by parallel methods implemented in PETSc library. The details on numerical method may be found in [12].

2.3 Flow parameters and computation domain

Computations are carried out at free-stream Mach number $\mathrm{M}_\infty = 5.373$, the unit Reynolds number $\mathrm{Re}_{\infty,1} = V_\infty^* \rho_\infty^* / \mu_\infty^* = 17.8\times10^6\ \mathrm{m}^{-1}$, $\gamma = 1.4$, $\mathrm{Pr} = 0.72$, $T_\infty^* = 74.194\,\mathrm{K}$. The wall is isothermal with $T_w^* = 300.0\,\mathrm{K}$, i.e. $T_w = 4.043$, and the ratio to the adiabatic wall temperature is $T_w / T_{aw} \simeq T_w^* / \left[T_\infty^* \left(1 + \sqrt{\mathrm{Pr}}\,\tfrac{1}{2}(\gamma-1)M_\infty^2\right)\right] = 0.685$ (not too "cold" wall). These flow parameters are the same as in [5, 11] and relevant to the stability experiments of NASA X-43 model [4]. The reference length scale $L^* = 0.3161$ m corresponds to the distance from the leading edge to the corner line, that gives the Reynolds number $\mathrm{Re}_\infty = L^*\,\mathrm{Re}_{\infty,1} = 5.667\times10^6$.
Computations are carried out for the flow over a long $5.5°$ compression ramp. The computation domain in (x, y) plane is shown in figure 1. It is extruded along the spanwise z-axis to obtain the 3D domain with the spanwise range of $0 \le z \le 0.2$.
The boundary conditions are: no-slip conditions $u = v = w = 0$ and $T = T_w$ on the wall (bottom $y = y_{\min}$ boundary); the free-stream conditions $u = 1$, $v = w = 0$, $p = 1/\gamma \mathrm{M}_\infty^2$, $T = 1$ on the $x = x_{\min} = 0$ (left) and $y = y_{\max}$ (top) boundaries; the linear extrapolation from the interior for the dependent variables u, v, w, p and T on the $x = x_{\max} = 4$ (right) boundary; the symmetry condition ($\partial u/\partial n = \partial v/\partial n = \partial p/\partial n = \partial T/\partial n = 0$, $w = 0$) at $z = 0$.

DOI: 10.13009/EUCASS2017-656

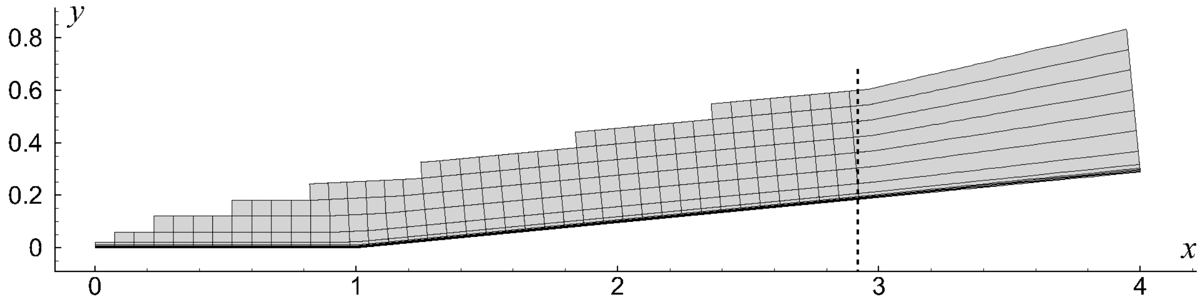

Figure 1: Computational domain in (x, y) plane. The solid lines show the edges of grid blocks. The dashed line shows the inflow boundary of the buffer zone

An orthogonal grid with $6001 \times n_y \times 151$ nodes (223×10^6 in total) was used for simulations. The number of nodes in vertical direction n_y varies from 126 to 376 through the computational domain depending on the bow shock location. The nodes are clustered near the surface so that about 120 grid lines are within the boundary layer with the constant cell size $\Delta y = 1\times10^{-4}$. In the streamwise and spanwise directions the grid is equidistant with the cell sizes $\Delta x = 5\times10^{-4}$ and $\Delta z = 13\times10^{-4}$ respectively. Note that the Kolmogorov microscale (size of the smallest eddies) is $l_K \sim \mathrm{Re}_\infty^{-3/4} = 0.086\times10^{-4}$, and the Taylor microscale (size of the eddies in the inertial subrange) is $l_T \sim \sqrt{10}\,\mathrm{Re}_\infty^{-1/2} = 13\times10^{-4}$.
Near the outflow boundary the size of last 160 grid cells is gradually increased up to $\Delta x = 0.1$. This part of computational domain acts as a "buffer" ("sponge") zone where the unsteady disturbances dissipates via numerical viscosity.

2.4 Disturbances actuator

The problem is solved in two steps. First, a steady laminar flow field (base flow) is computed using the time-dependent method. Then, unsteady disturbances are imposed onto the base flow via the actuator modelled as boundary condition for the vertical mass-flow perturbation

$$(\rho v)_w = \varepsilon \sin\left(2\pi \frac{x - x_1}{x_2 - x_1}\right) \sin\left(\pi \frac{z - z_1}{z_2 - z_1}\right) \sin\left(\omega_0 t\right),$$
$$x_1 \le x \le x_2,\; z_1 \le z \le z_2,\; 0 \le t \le t_1. \qquad \textbf{(1)}$$

Here $x_1 = x_0 - d$, $x_2 = x_0 + d$, $z_1 = -d/2$, $z_2 = d/2$ are boundaries of the forcing region with central point $x_0 = 0.04395$ and size $d = 0.00815$. This condition imitates a blow–suction through 2 adjacent holes. The frequency of the actuator is set to relatively low value $\omega_0 = 125$ (corresponding frequency parameter is $F_0 = \omega_0 / \mathrm{Re}_\infty = 2.206\times10^{-5}$) typical for the first-mode instability, which was estimated in [11] using linear stability theory [1]. To ensure linear evolution of the disturbances in the region $x_0 < x < 1$ upstream the separation, the forcing amplitude is chosen small $\varepsilon = 10^{-3}$.
Considered are two cases of the forcing duration t_1: 1) half of period $t_1 = \pi / \omega_0$ for wave packet generation and 2) infinity $t_1 = \infty$ for wave train. The induced wave packet develops downstream into a turbulent spot, while wave train produce a turbulent wedge.

3. Results

3.1 Steady base flow

The computed laminar steady-flow field (base) over the ramp is shown in figure 2. The viscous-inviscid interaction leads to formation of a weak shock wave in the leading-edge vicinity. The vertical size of the computational domain is chosen so that the shock wave does not intersect the upper boundary to avoid non-physical reflections. In the

DOI: 10.13009/EUCASS2017-656

corner region, there are compression waves interacting with the boundary layer and inducing a shallow recirculation zone – a separation bubble. Using the skin friction coefficient distribution

$$c_{f,x} = \tau^*_{w,x} \Big/ \tfrac{1}{2}\rho^* V^*_\infty = 2\left[\mu \frac{\partial u}{\partial n}\right]_w \Big/ \mathrm{Re}_\infty ,$$

the coordinates of separation and reattachment points are detected as $x_{sep} = 0.857$ and $x_{att} = 1.136$ respectively.

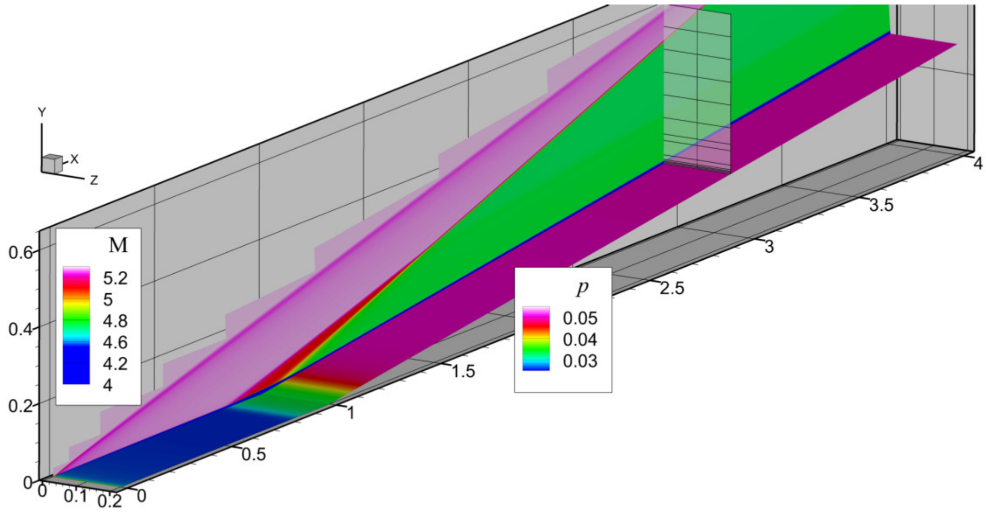

Figure 2: Steady flow over the compression ramp. Mach numbers field in the symmetry plane and pressure field on the wall. The vertical plane at x = 2.92 mark the beginning of “buffer” zone

3.2 Simulation of a turbulent spot

A turbulent spot is excited by the wave packet, which is generated by a short pulse $t_1 = \pi / \omega_0 = 0.014$ of the actuator (1). Such forcing has spectrum containing wide range of frequencies and wavenumbers, including plane high-frequency components relevant to the second-mode waves, as well as oblique low-frequency components associated with the first mode.

Figure 3 illustrates the downstream propagation of the wave packet over the compression ramp. Shown are the instantaneous contours of the wall-pressure disturbance at several time instants. Hereafter the disturbance fields $p'(t)$ are obtained by subtracting the base flow field from the field at a particular time instant, i.e. $p'(t) = p(t) - p(t = 0)$. The vertical lines indicate locations of the separation, corner and reattachment lines.

Initially the waves emanating from the forced area are elliptic. As the disturbance propagates in the region upstream of separation, a V-shaped tail is formed while the wave packet core exhibits a staggered 3D pattern (figure 3, t = 0.9). This is typical for the disturbance dominated by the oblique waves relevant to the first mode instability.

The wave packet crosses the separation line x_{sep} = 0.857 without noticeable changes of its structure (figure 3, t = 1.1). Further downstream, it quickly elongates in the streamwise direction – the fore part of disturbance moves faster than its rear part located in the separation region (figure 3, t = 1.5).

Far downstream the reattachment line (x_{att} = 1.136) nonlinear breakdown occurs (figure 3, t = 2.0), and then the wave packet transforms to a “young” turbulent spot with small scale random-like structures in the core part (figure 3, t = 3.0). This is also illustrated in figure 4 by vortices identified by Q-criterion. Small-scale hairpin structures fill up the central portion of the turbulent spot surrounded by oblique waves, while the disturbance tail consists of longitudinal structures elongated downstream.

The side view of the turbulent spot is shown in figure 5 using the shadowgraph visualization (density Laplacian $\nabla^2\rho$) in the symmetry plane $z = 0$. Small-scale random structures are observed in the near-wall region, while the disturbance field in the outer part of boundary layer is dominated by large-scale structures. Outside the disturbed boundary layer the waves are clearly seen, that resembles the acoustic noise from the turbulent flow.

DOI: 10.13009/EUCASS2017-656

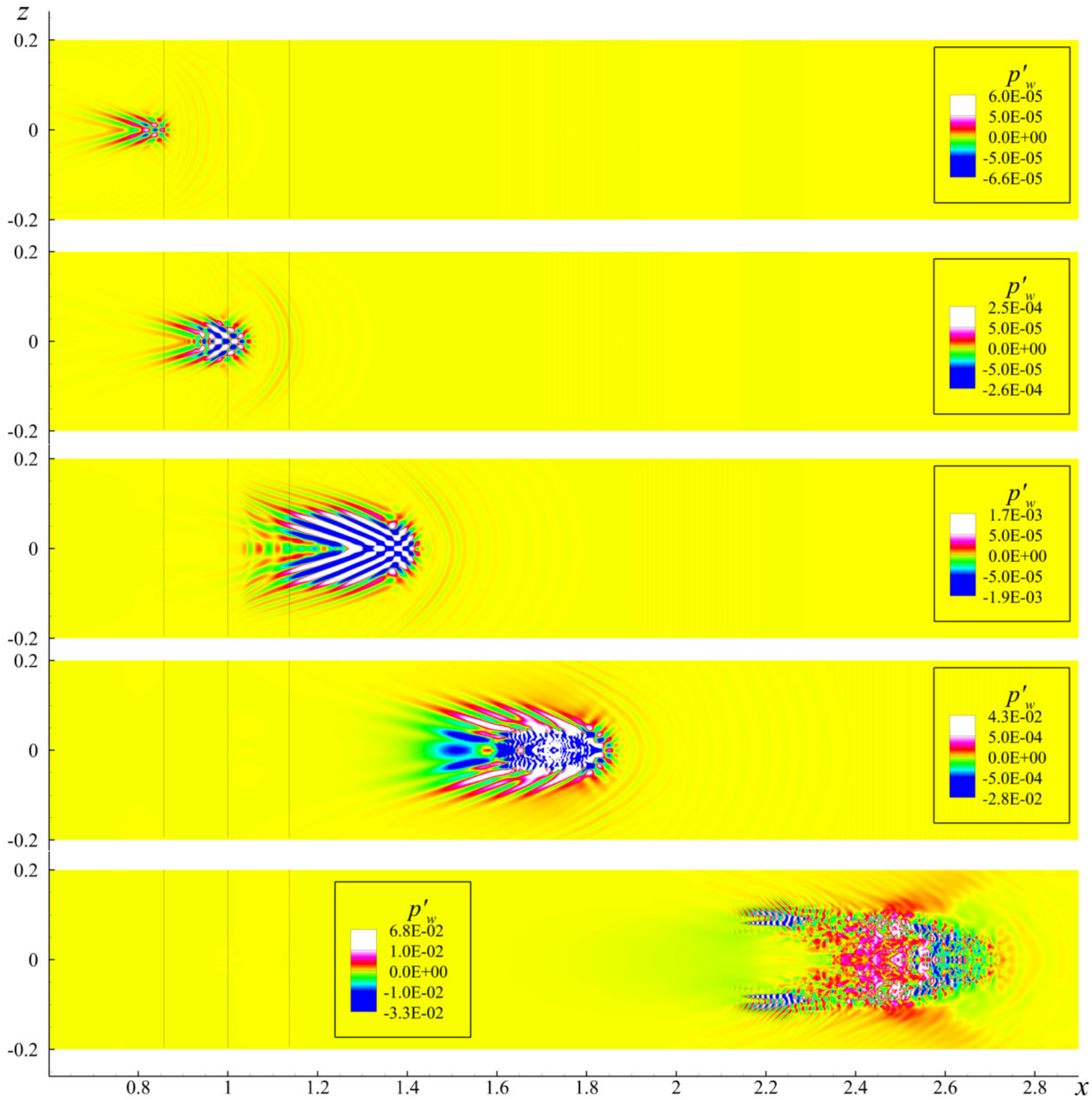

Figure 3: Wall pressure disturbances at the time instants t = 0.9; 1.1; 1.5; 2.0; 3.0

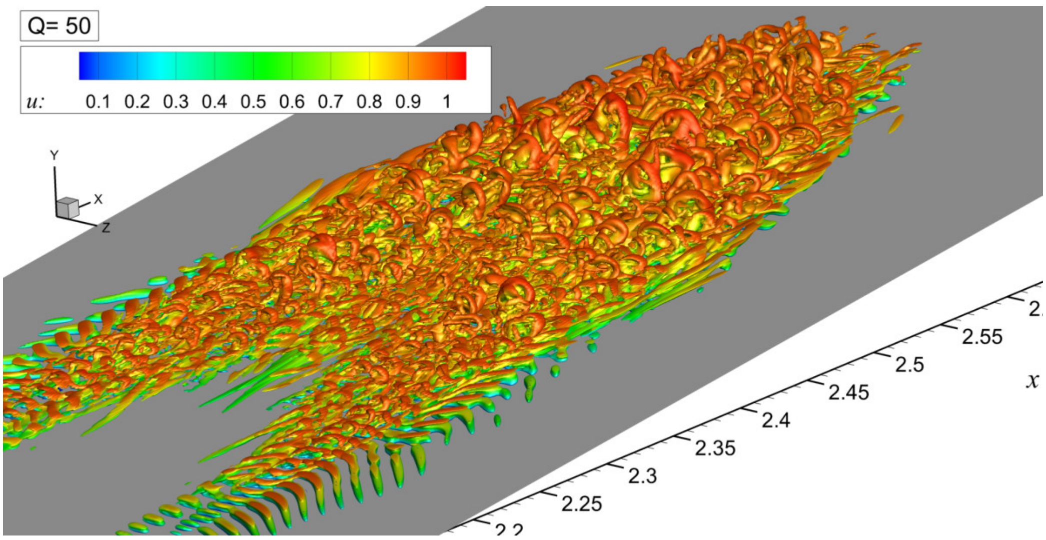

Figure 4: Visualization of vortices by Q-criterion at t = 3.0. The isosurface is colored using the u-velocity magnitude

DOI: 10.13009/EUCASS2017-656

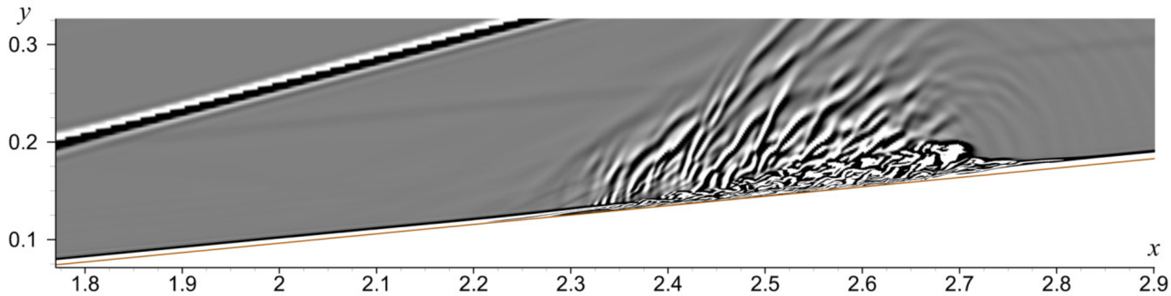

Figure 5: Shadowgraph in the symmetry plane $z = 0$ at $t = 3.0$ for the young turbulent spot

3.3 Simulation of a turbulent wedge

A turbulent wedge is induced by the wave train, which is generated by the suction-blowing actuator (1) working permanently (duration $t_1 = \infty$).

Figure 6 shows the pressure disturbance field on the wall at the time instant $t = 5.3$ when the transient process associated with the generator switching-on have already finished. In the linear stage, the wave train is harmonic with its frequency being equal to the forcing frequency at any fixed point in space. In the nonlinear breakdown stage, the disturbance evolves to a stationary stochastic state with its mean characteristics being constant versus time.

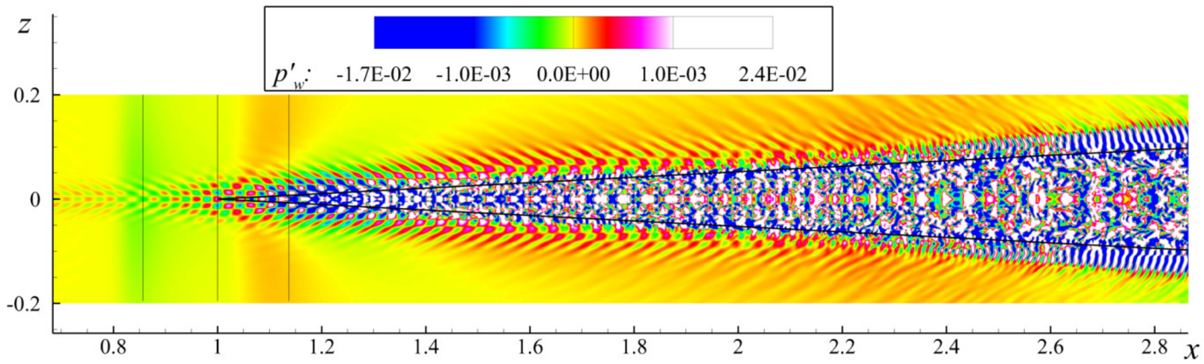

Figure 6: Wall pressure disturbances for turbulent wedge case. Straight black lines mark the core part of the wedge

In the linear stage upstream the separation $x < 0.8$ the wave train consist of oblique waves with the front angle being about $66°$ in agreement with the LST assessments reported in [11]. These waves form a V-shape pattern typical for the first-mode dominated disturbance.

The disturbance grows monotonically until the nonlinear breakdown occurs. Starting from the station $x \approx 2.25$ the wave train core exhibits a stochastisation. Here a "young" turbulent wedge is formed. It's lateral spread is characterised by the half-angle $\varphi \approx 3°$, that is the same as for turbulent spots observed in experiments [13] and DNS [14].

The side view of the turbulent wedge is shown in figure 7 using the shadowgraph visualization in the symmetry plane $z = 0$. Small-scale random-like structures are observed in the near-wall region, while the disturbance field in the outer part of boundary layer is dominated by almost periodic large-scale structures. This topology is consistent with the well-known experimental fact that stochastisation of the boundary-layer flow begins near the wall. Waves outside the disturbed boundary layer resemble the acoustic noise from the turbulent flow.

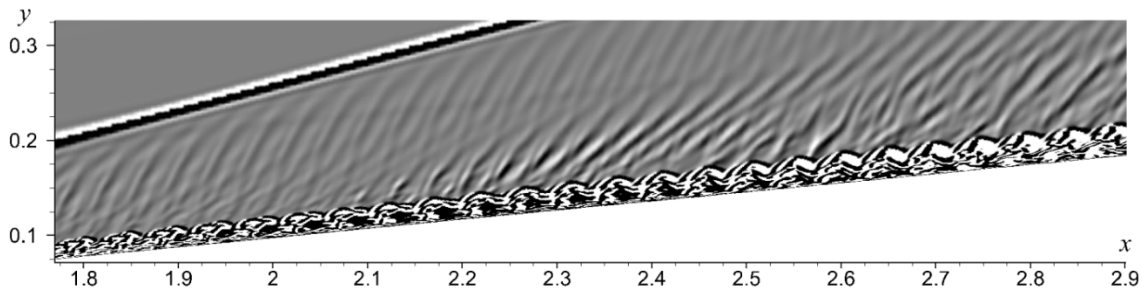

Figure 7: Shadowgraph in the symmetry plane $z = 0$ at $t = 3.0$ for the young turbulent wedge

DOI: 10.13009/EUCASS2017-656

Spatial vortical structures at the late stage of transition are shown in figure 8. Here the vortices are identified by Q–criterion. Small-scale hairpin vortices fill up the central portion of the wave train surrounded by oblique waves. Hairpin vortices are arranged straight in a line, which is relevant to the fundamental or/and oblique breakdown scenarios but not the subharmonic one. In a whole, there are vortices of many scales that are typical for turbulent boundary layers. However, still visible regular-in-space structures indicate that the flow is not fully turbulent.

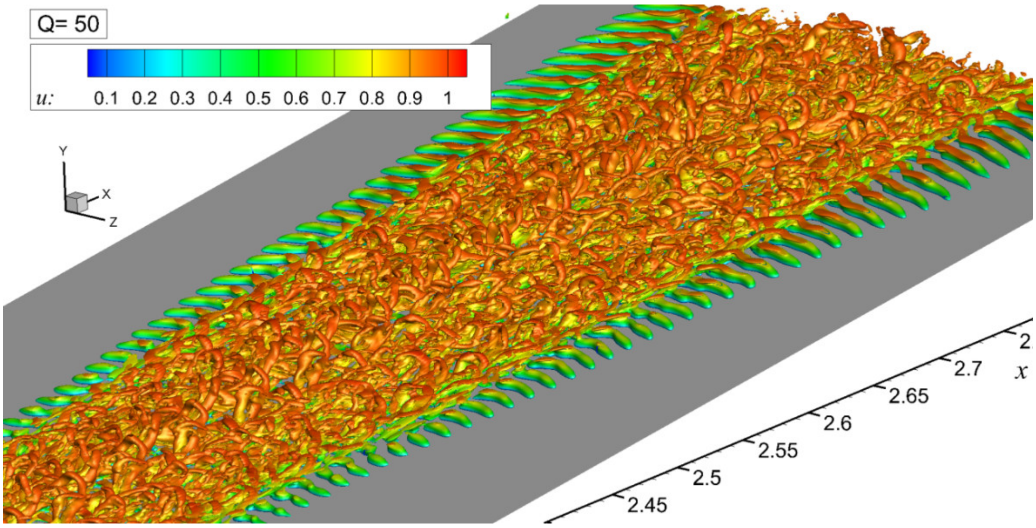

Figure 8: Visualization of vortices by Q–criterion in the turbulent wedge. The isosurface of Q is coloured with the u-velocity magnitude

The beginning of LTT and the streamwise length of transitional region can be assessed using the distribution of heat transfer coefficient – the Stanton number. Herein the Stanton number is calculated as

$$St = \frac{\mu_w}{\mathrm{Re}\,\mathrm{Pr}} \frac{1}{T_0 - T_w} \left(\frac{dT}{dn} \right)_w ,$$

which is valid for perfect gas. Instantaneous field of $St(x,z)$ at time instant $t = 5.3$ is shown in figure 9. Starting from the station $x \approx 1.2$ the heat transfer increases that is typical for the LTT process. The growth varies versus z so that streaky structures are seen in the $St(x,z)$ pattern.

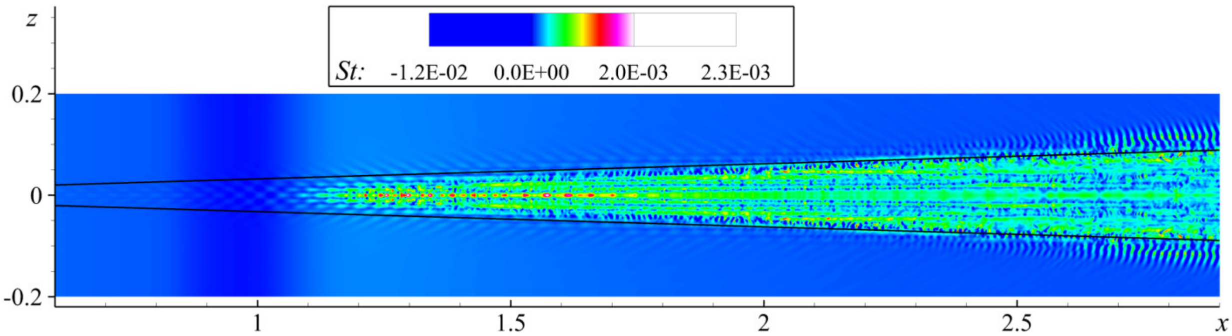

Figure 9: Heat transfer coefficient *St(x,z)* at time instant *t* = 5.3 for the turbulent wedge. Straight black lines indicate limits for spanwise averaging

Figure 10 shows the distribution of heat transfer $St(x)$ along the centreline $z = 0$ and the distribution of $\langle St(x) \rangle_z$ averaged over z-coordinate. The z-averaging is performed over the core part of wave train marked by solid black lines in figure 9. It is seen that the $St(x)$ distribution along the centreline $z = 0$ exhibit significant overshoot past relaxed values. DNS [15] of transitional hypersonic boundary layer on a flat plate at Mach 6 showed that such overshoots are due to the interaction of oblique modes which leads to the generation of strong streamwise vorticity.

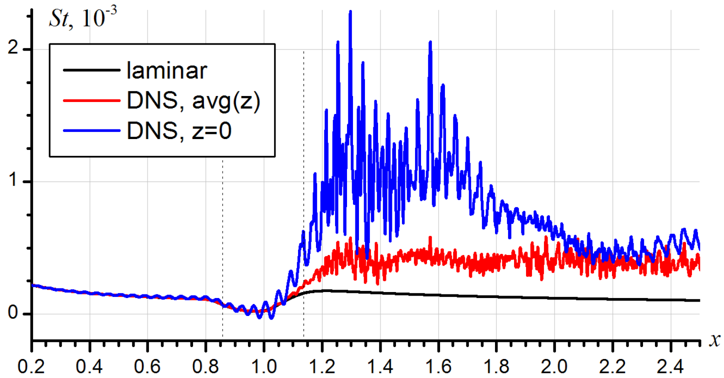

Figure 10: Heat transfer coefficient distribution along x-coordinate at $t = 5.3$ for the wave train. "laminar" − steady unperturbed base flow; "DNS, avg(z)" – spanwise averaging; "DNS, z=0" –in the symmetry plane z=0

4. Conclusion

Direct numerical simulations were performed for the transitional boundary layer flow with local separation zone over the sloped plate at the freestream Mach number M_∞ = 5.373 and unit Reynolds number $Re_{\infty,1} = 17.8 \times 10^6$ m^{-1} relevant to the experiments on NASA X-43 hypersonic glider. The laminar-turbulent transition is induced by artificial disturbances generated using a pulsed or periodic local in space forcing of the vertical mass-flow on the wall near the leading edge. The forcing frequency was chosen to be relevant to the first-mode instability predicted by the linear stability theory. The forcing level was chosen to be sufficiently small to simulate linear, weakly nonlinear and transitional stages of the disturbance development.

Computations were carried out using the in-house Navier–Stokes solver HSFlow that implements an implicit finite-volume shock-capturing method with the 2nd order approximation in time and effectively 3rd order approximation in space. Despite of the dissipative nature of this quasi-monotone numerical scheme, it is feasible to simulate the disturbance development from the linear stage to the "young" turbulent spot or wedge, provided the appropriate grid resolution.

In the linear stage the low frequency disturbance is dominated by oblique waves of the first mode. These waves are amplified until the nonlinear breakdown occurs and "young" turbulent spot or wedge is formed. The turbulent wedge over the sloped plate has lateral spread with half-angle $\varphi \approx 3°$, that is relevant to experimental values.

In the late stage of nonlinear disturbance evolution, the boundary layer exhibits small-scale random-like structures in the near-wall region. The acoustic waves are emitted to the outer flow that resembles the noise of turbulent boundary layer. Hairpin vortices fill up a central portion of the disturbance surrounded by oblique waves. The mean boundary layer flow restructures and longitudinal vortices (near-wall streaks) are observed in the pattern of the heat transfer coefficient field. The heat transfer distribution along the centreline of transitional boundary layer exhibit significant overshoot past relaxed values – a clear indication that the oblique breakdown plays important role in the transition process.

In summary, this and similar numerical simulations may help to setup and perform controlled experiments in quiet hypersonic wind tunnels as well as develop holistic models of transitional boundary layer at hypersonic speeds.

Acknowledgments

This work was carried out at Moscow Institute of Physics and Technology (MIPT) using high-performance computing resources of Federal Centre for Collective Usage at NRC "Kurchatov Institute" (http://computing.kiae.ru) with financial support of the Russian Scientific Foundation (Project No. 14-19-00821; sections 1, 2, 3.1, 3.3 and 4) and the Russian Foundation for Basic Research (project No. 16-08-01200; section 3.2).

References

[1] Fedorov, A. 2011. Transition and Stability of High-Speed Boundary Layers. *Annu. Rev. Fluid Mech.* 43:79–95.

[2] Zhong, X., and Wang, X. 2012. Direct Numerical Simulation on the Receptivity, Instability, and Transition of Hypersonic Boundary Layers. *Annu. Rev. Fluid Mech.*, 44:527–561.

DOI: 10.13009/EUCASS2017-656

[3] Fasel, H. F. 2011. Numerical Simulation of Transition in Hypersonic Boundary Layers. Report AFRL-OSR-VA-TR-2012-0255, AFOSR/RSA.

[4] Berry, S. A., DiFulvio, M., and Kowalkowski, M. K. 2000. Forced Boundary Layer Transition on X-43 (Hyper-X) in NASA LaRC 20-Inch Mach 6 Air Tunnel. Report NASA TM-2000-210316.

[5] Balakumar P., Zhao, H., and Atkins, H. 2005. Stability of hypersonic boundary layers over a compression corner. *AIAA J.*, 43(4):760–767

[6] Egorov I. V., Novikov, A. V., and Fedorov, A. V. 2006. Numerical modelling of the disturbances of the separated flow in a rounded compression corner. *Fluid Dynamics*. 41(4):521–530.

[7] Zhao, H., and Balakumar, P. 2005. Nonlinear disturbance evolution across a hypersonic compression corner. *AIAA J.*, 43(5):1034–1041.

[8] Novikov, A., Egorov, I., and Fedorov, A. 2016. Direct numerical simulation of wave packets in hypersonic compression-corner flow. *AIAA J.*, 54(7):2034–2050.

[9] Novikov, A. V., Egorov, I., and Fedorov, A. V. 2016. Numerical Study of Wave Trains in Supersonic Flow over a Compression Corner. AIAA paper 2016-0049.

[10] Novikov, A.V., and Egorov, I. 2016. Direct Numerical Simulations of Transitional Boundary Layer over a Flat Plate in Hypersonic Free-Stream. AIAA paper 2016-3952.

[11] Novikov, A. V. 2017. Transition Induced by a Wave Train in a Supersonic Boundary Layer over a Compression Ramp. AIAA paper 2017-4517.

[12] Egorov, I.V., and Novikov, A. V. 2016. Direct numerical simulation of laminar–turbulent flow over a flat plate at hypersonic flow speeds. *Computational Mathematics and Mathematical Physics*. 56(6):1048–1064.

[13] Fischer, M.C. 1972. Spreading of a turbulent disturbance. *AIAA Journal*. 10(7):957–959.

[14] Redford, J.A., Sandham, N.D., and Roberts, G.T. 2012. Numerical simulations of turbulent spots in supersonic boundary layers: Effects of Mach number and wall temperature. *Progress in Aerospace Sciences*. 52:67–79.

[15] Franko, K.J., Bhaskaran, R., and Lele, S. K. 2011. Direct Numerical Simulation of Transition and Heat-transfer Overshoot in a Mach 6 Flat Plate Boundary Layer. AIAA paper 2011-3874.